Ultrasound in Medicine & Biology 50 (2024) 1214–1223

Contents lists available at ScienceDirect

Ultrasound in Medicine & Biology

journal homepage: www.elsevier.com/locate/ultrasmedbio

Original Contribution

Nanoparticle-Mediated Histotripsy Using Dual-Frequency Pulsing Methods

Connor Edsall [a,*], Laura Huynh [b], Waleed Mustafa [c], Timothy L. Hall [d], Yasemin Yuksel Durmaz [c,e], Eli Vlaisavljevich [a,f]

[a] Department of Biomedical Engineering and Mechanics, Virginia Polytechnic Institute and State University, Blacksburg, VA, USA
[b] Department of Materials Science and Engineering, Virginia Polytechnic Institute and State University, Blacksburg, VA, USA
[c] Department of Biomedical Engineering, Istanbul Medipol University, İstanbul, Turkey
[d] Department of Biomedical Engineering, University of Michigan, Ann Arbor, MI, USA
[e] Research Institute of Health Science and Technologies (SABITA), Istanbul Medipol University, Istanbul, Turkey
[f] ICTAS Center for Engineered Health, Virginia Polytechnic Institute and State University, Blacksburg, VA, USA

ARTICLE INFO

Keywords:
Histotripsy
Dual-frequency
Nanoparticle-mediated histotripsy
Nanoparticles
Cavitation
Ablation
Nanocone clusters

ABSTRACT

Objective: Nanoparticle-mediated histotripsy (NMH) is a novel ablation method that combines nanoparticles as artificial cavitation nuclei with focused ultrasound pulsing to achieve targeted, non-invasive, and cell-selective tumor ablation. The study described here examined the effect of dual-frequency histotripsy pulsing on the cavitation threshold, bubble cloud characteristics, and ablative efficiency in NMH. High-speed optical imaging was used to analyze bubble cloud characteristics and to measure ablation efficiency for NMH inside agarose tissue phantoms containing perfluorohexane-filled nanocone clusters, which were previously developed to reduce the histotripsy cavitation threshold for NMH.

Methods: Dual-frequency histotripsy pulsing was applied at a 1:1 pressure ratio using a modular 500 kHz and 3 MHz dual-frequency array transducer. Optical imaging results revealed predictable, well-defined bubble clouds generated for all tested cases with similar reductions in the cavitation thresholds observed for single-frequency and dual-frequency pulsing.

Results: Dual-frequency pulsing was seen to nucleate small, dense clouds in agarose phantoms, intermediate in size of their component frequencies but closer in area to that of the higher component frequency. Red blood cell experiments revealed complete ablations were generated by dual-frequency NMH in all phantoms in <1500 pulses. This result was a significant increase in ablation efficiency compared with the ~4000 pulses required in prior single-frequency NMH studies.

Conclusion: Overall, this study indicates the potential for using dual-frequency histotripsy methods to increase the ablation efficacy of NMH.

Introduction

Nanoparticle-mediated histotripsy (NMH) is a targeted ablation method being developed for the non-invasive treatment of cancer and other clinical applications [1–5]. NMH generates characteristic cavitation bubble clouds at pressures significantly below the histotripsy intrinsic threshold by exposing exogenous, artificial nanoparticles to histotripsy pulsing [1–3,6,7]. Histotripsy is an established non-invasive, non-thermal ultrasound ablation method currently under pre-clinical and clinical development for numerous indications [8]. Intrinsic threshold histotripsy (ITH) is a form of histotripsy that uses 1 to 2 cycle pulses with high peak negative pressures ($p-$ >25 MPa) to generate bubble clouds from *de novo* cavitation nuclei that are intrinsic to the medium [9–11]. Instead of relying on these *de novo* cavitation nuclei, NMH uses perfluorocarbon (PFC) fluid-filled nanoparticles to generate cavitation at lower peak negative pressures ($p-$ <12 MPa) resulting from the nucleation threshold of the PFC inside the particles [3,5,6,12–14]. This reduced cavitation threshold allows for targeted nucleation of histotripsy bubbles isolated to regions containing the nucleating agent, thus minimizing the need for high-pressure pulsing and image-guided targeting to create successful ablations [1,4,6].

This work builds on our previous studies in which we developed NMH using perfluorohexane (PFH)-filled nanocone clusters (NCCs) to reduce the histotripsy cavitation threshold [3,5–7]. NCCs are a self-organized structure of inclusion complexes of β-cyclodextrin (BCD) and PFH with a size of ~40 to 100 nm and reported $p-$ thresholds of ~9 to 11 MPa when exposed to 500 kHz histotripsy pulsing [3,5,6]. Recent work has also revealed that NMH from NCCs sustainably generates

* Corresponding author. Department of Biomedical Engineering and Mechanics, Virginia Polytechnic Institute and State University, 325 Stanger Street, Blacksburg, VA 24061, USA.
E-mail address: cwedsall@vt.edu (C. Edsall).

https://doi.org/10.1016/j.ultrasmedbio.2024.04.009
Received 14 November 2023; Revised 19 April 2024; Accepted 21 April 2024

bubble clouds over successive pulses capable of producing effective histotripsy ablation but with a reduced ablation efficiency compared with ITH at the same pulse frequency [4,6]. For instance, prior studies determined that 500 kHz ITH results in complete ablation of the focal volume in 300–1000 pulses [6,15], whereas NMH achieved ~70% ablation only following 2000 pulses when using the same pulsing parameters at lower pressures (20 MPa vs. >38 MPa) [6]. Histotripsy ablation efficiency, defined as the number of pulses required to remove the focal area occupied by the bubble cloud, has been reported to directly correlate with the size of the individual bubbles constituting the cloud and the number of bubbles nucleated within the focal area [6,16]. The reduced ablation efficiency in NMH has been hypothesized to result from reduced bubble expansion caused by the lower applied pressure required for generating the cavitation clouds in NMH [1,6,17,18]. This hypothesis is based on several prior studies indicating that histotripsy ablation capacity depends on the magnitude and rate of strain applied to the tissue through the rapid growth and collapse of bubbles within the target tissue [17–21]. This hypothesis is supported by a recent study from our group finding that ablation from exogenous nuclei, such as the NCCs used in NMH, is less efficient because of the reduced maximum bubble radius (R_{max}) produced from the bubbles at these lower pressures [6]. However, as prior studies also report that ablation efficiency depends on the number of bubbles generated within the focal region (*i.e.,* the bubble cloud density), we hypothesize that alternate pulsing strategies can be developed to enhance NMH treatment efficiency to compensate for the reduction in efficiency caused by the lower acoustic pressures.

In this study, we investigated use of a single-cycle, dual-frequency (500 kHz:3 MHz) pulsing method to enhance ablation efficiency in NMH. This dual-frequency, single-cycle histotripsy pulsing strategy was previously developed to modulate individual bubble expansion and alter bubble cloud size by changing the percentage of pressure applied by the respective frequencies [11,22,23]. Although other methods of dual- and multi-frequency pulsing have been investigated for potential therapeutic enhancement in both thermal and mechanical focused ultrasound [24–26], the underlying mechanisms of action involved in this study are possible only for single-cycle pulsing methods in which the peak negative pressures of the respective frequencies are precisely aligned at the focus. More specifically, this work builds directly on a recent ITH study by our group indicating that dual-frequency histotripsy pulsing using precisely aligned single-cycle pulses of two different frequencies can modulate bubble cloud dimensions and density, potentially enhancing ablation efficiency [22]. Here, we characterize the bubble cloud characteristics and resulting ablation produced by dual-frequency NMH inside agarose tissue phantoms containing NCCs. The histotripsy cavitation threshold, bubble cloud characteristics, and ablation efficiency in tissue phantoms containing NCCs were captured and quantified using high-speed optical imaging. We hypothesized that dual-frequency pulsing would retain NMH's significantly reduced cavitation threshold and produce predictable bubble clouds matching the area of the focus above the NMH cavitation threshold. We further hypothesized that dual-frequency pulsing would result in more rapid ablation of the focal area (compared with single frequencies) because of the increased bubble cloud density from the higher-frequency component and enhanced bubble expansion from the lower-frequency component reported in a prior study [22]. Overall, the results of this study will establish the feasibility of using dual-frequency pulsing to enhance NMH ablation capabilities, provide greater insight into the NMH ablative process, and further the development of NMH as a potential non-invasive ablative therapy.

Methods

Histotripsy Pulse Generation and Experimental Setup

With the same scaffold and experimental setup employed in our previous studies [6,15], a 32-element array transducer with an aperture of 120.5 mm and a geometric focus of 75 mm, producing an *f*-number of 0.62 was used for all experiments in this study. The transducer's three concentric rings of 6, 12, and 14 elements were populated by sixteen 500 kHz and sixteen 3 MHz circular focused (20 mm diameter) modular elements in an evenly distributed alternating pattern (Fig. 1B). The transducer was fixed horizontally in a tank of degassed, deionized (DI) water (<26% dissolved oxygen), and a MATLAB (The MathWorks, Natick, MA, USA)-controlled computer-guided 3-D positioning system oriented the tissue phantoms and hydrophones to the focus (Fig. 1A).

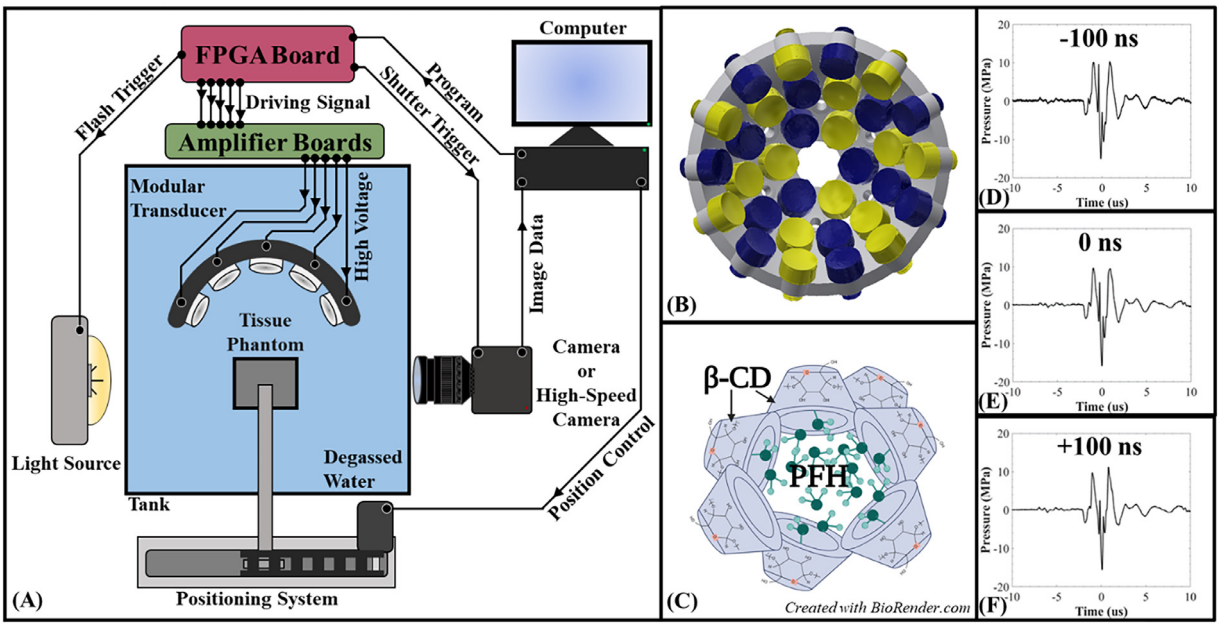

Figure 1. Dual-frequency histotripsy experimental setup and nanocone cluster schematic. (A) Optical imaging captured cavitation behavior and red blood cell (RBC) ablation efficiency inside 1% agarose tissue phantoms exposed to dual-frequency histotripsy pulses applied by the modular 32-element modular transducer (B) populated by alternating 3 MHz (*yellow*) and 500 kHz (*blue*). (C) Nanocone clusters (NCCs) were dispersed in all agarose gels. (D–F) Gels were exposed to dual-frequency pulsing of a 1:1 pressure ratio of 500 kHz and 3 MHz with three different 3 MHz pulse arrival times relative to the 500 kHz pulse of −100 ns (D), 0 ns (E), and +100 ns (F). FPGA, field-programmable gate array.

MATLAB also programmed a field-programmable gate array (FPGA) board (Altera DE0-Nano Terasic Technology, Dover, DE, USA) to simultaneously control triggering of the camera, strobe and therapy pulsing. The FPGA was programmed to deliver short histotripsy therapy pulses of <2 cycles through a custom high-voltage amplifier populated by interchangeable boards (four 3 MHz and four 500 kHz) matched to the respective element frequencies.

Hydrophone Focal Pressure Calibration

A custom fiberoptic hydrophone (FOPH) [27] was cross-calibrated at nine low-pressure values (0–5 MPa peak to peak) with a high-sensitivity reference hydrophone (HNR-0500, Onda Corp., Sunnyvale, CA, USA) to ensure accurate pressures were measured from the FOPH. The FOPH measured focal pressure waveforms for both the 500 kHz and 3 MHz elements in degassed water (~26% dissolved O_2) at the focal point of the transducer, which was identified using 0.1 mm incremented 1-D axial, transverse and elevational scans of the focus. The phase of all the elements was controlled so that the $p-$ of the 3 MHz pulse aligned with the $p-$ of the 500 kHz pulse. Focal pressures of the individual frequencies were directly measured up to a peak negative pressure ($p-$) of 18 MPa and estimated for higher pressure levels ($p-$ >20 MPa) by summing measurements from subsets of 16 elements (eight 3 MHz and eight 500 kHz). Respective voltage levels corresponding to the same $p-$ were matched for the 500 kHz and 3 MHz elements. The focal pressures for the combined, centered (0 ns) dual-frequency pulses were taken following the same process. This process was repeated for the $p-$ of the 3 MHz pulse aligned 100 ns before (−100 ns) and after (+100 ns) the 500 kHz pulse arrival. All waveforms were captured with a Tektronix TBS2000 series oscilloscope (Tektronix, Inc., Beaverton, Oregon, USA) at a sample rate of 500 MS/s, and the waveform data was averaged over 512 pulses and recorded in MATLAB. Figure 1D, 1E and 1F are example averaged acoustic waveforms measured by the FOPH for each arrival time of the 3 MHz pulse relative to the 500 kHz pulse.

Formulation of Perfluorohexane-filled Nanocone Clusters

Nanocone clusters (Fig. 1C) are self-organized structures of inclusion complexes of β-cyclodextrin (BCD) and PFH around free PFH molecules in an aqueous environment. These were prepared with an optimized method similar to that described recently [5,7]. Briefly, BCD (100 mg, 8.8×10^{-2} mmol) was dissolved completely in double-distilled water (6 mL) at room temperature, followed by the addition of PFH at the optimized molar ratio of 1:5 (BCD:PFH). After overnight stirring, the NCC aggregates, including the inclusion complex of PFH and BCD as building blocks around free PFH, precipitate and can be separated by simple filtration or centrifugation and then dried in a vacuum to form a solid white powder. The PFH content of the obtained powder was calculated using gas chromatography through a calibration curve containing different concentrations of free PFH. Further evidence for the presence of the PFH was confirmed using scanning electron microscopy with energy-dispersive X-ray analysis (SEM-EDAX).

Agarose–NCC Phantom Preparation

Agarose tissue phantoms (1% w/v) have previously been reported to provide an optically clear medium closely matching mechanical and viscoelastic material properties of most principal tissue targets for histotripsy [19]. The phantoms were prepared using previously published methods [6]. Saline solution (0.45%) was prepared using DI water degassed using a Portable Water Degasser (DS-50, FUS Instruments, Toronto, ON, Canada). The agarose gel was then made by mixing 0.6% agarose powder (Type VII-A, Sigma Aldrich, St. Louis, MO, USA) with 99.4% of a 0.45% saline solution at room temperature. The agarose was fully dissolved by heating the mixture in a microwave until boiling and then stirring. The solution was degassed by repeatedly heating it to boiling and stirring quickly to cause flash boiling, releasing dissolved gas from the mixture until 50% of the volume remained, yielding a degassed 1.2% (w/v) agarose gel with 0.9% saline content. The mixture was placed under a partial vacuum (~33.62 kPa, absolute) for ~25 min to remove any remaining gas and minimize re-gassing as the agarose solution cooled. The pressure was then decreased to ~16.75 kPa to force any remaining gas from solution until the solution had cooled to 40°C.

Desiccated NCC powders were mixed with 20 mL of degassed 0.9% saline, forming a solution with an NCC concentration of 6×10^{-5} mL PFH/mL water The degassed saline and NCC solution were then stirred at 500 rpm for ~20 min in a desiccator under ~33.62 kPa absolute pressure to disperse the NCCs fully. Once the temperature of the degassed agarose was 40°C, a serological pipet was used to slowly add 100 mL of the solution into a custom-designed PLA frame (76.2 mm [H] × 38.6mm [D] × 45.2mm [W]) inside a rectangular silicone mold. Twenty milliliters of NCCs in degassed 0.9% saline was incorporated by gentle stirring with the end of the serological pipet. The resulting phantom was 120 mL of 1% (w/v) agarose containing NCCs with a final concentration of 10^{-5} mL PFH/mL water [3,6,7]. The prepared phantoms were placed in a refrigerator to solidify. Tests were performed within 2 h of creation to maintain the agarose concentration and degassed state of the gel.

Red Blood Bell Agarose–NCC Phantom Preparation

For ablation experiments, red blood cell (RBC) phantoms consisting of three layers of agarose containing NCCs, with the middle layer also containing 5% (v/v) red blood cells [1,6,15,28], were created. Fresh porcine blood was obtained from participants in an unrelated study and added to an anticoagulant solution of Citrate Phosphate Dextrose Anticoagulant (CPD, Sigma Aldrich Corp.), with a CPD-to-blood ratio of 1:9 mL. Whole blood was separated by centrifugation at 3000 rpm for 10 min. The plasma and white buffy coat were removed, and the RBCs were saved for addition to the phantom. The clear 1% agarose NCC top and bottom layers of the RBC phantom were created using the procedure described above. The base layer was pipetted at 40°C, and the housing was placed in a refrigerator at 4°C to allow the layer to completely cool and solidify. A second solution of 1% agarose–NCCs was produced using the same methods and its temperature was lowered to <38°C. Then 9.5 mL of the agarose solution was combined with 0.5 mL RBCs (5% v/v) by gentle inversion and poured on top of the chilled solidified agarose –NCC layer. The entire surface was quickly coated with the RBC–agarose–NCC solution before the excess solution was poured out, leaving behind a thin RBC-containing layer [3]. The whole phantom was replaced in the refrigerator. After 5 min, the RBC–agarose layer was solidified, and the remaining top layer of agarose–NCC solution was pipetted to fill the frame. This procedure created a thin layer of RBCs suspended in the center of the 1% agarose phantom containing NCCs throughout the ~15 mm (50 mL) thick top and bottom clear layers and the <0.25 mm thick center RBC layer.

Cavitation Detection Using Optical Imaging

Optical imaging captured images of the focal zone after the propagation of each pulse (Fig. 1A) using a machine vision camera (FLIR Blackfly S monochrome, BFS-U3-32S4M-C 3.2 MP, 118 FPS, Sony IMX252, Mono, FLIR Integrated Imaging Solutions, Richmond, BC, Canada) and a 100 mm F2.8 Macro lens (Tokina AT-X Pro, Kenko Tokina Co., LTD, Tokyo, Japan). This setup resulted in captured images with a resolution of 3.25 μm per pixel, with the camera triggered to record one image for each applied pulse during cavitation experiments. The tissue phantom was backlit by a custom-built pulsed white-light LED strobe capable of high-speed triggering of <1 μs. Strobe duration was kept as low as possible—2 μs for cavitation experiments to ensure minimal motion blur of the expanding bubbles while still sufficiently lighting the NCC-filled agarose. All exposures were centered at a delay of 3 μs after the peak

negative pressure arrived using the reference hydrophone and the oscilloscope. This delay was determined in pilot experimentation to be the time point that allowed the complete bubble cloud to form while attempting to minimize bubble coalescence or overlap from expanding individual bubbles. A custom computer program using image processing software (MATLAB) was employed to analyze the collected images using previously published methods [6,10,15,16] by converting each frame from grayscale to binary by an intensity threshold determined by the background intensity. Bubbles were indicated by any black regions >5 pixels resulting in a minimum resolvable bubble diameter of approximately 16 μm.

Cavitation Threshold Calculation and Comparison

For cavitation threshold experiments, 100 pulses were applied at incremental $p-$ levels ranging from 0 to 20 MPa to a single point 10 mm inside NCC containing tissue phantoms submerged inside a water tank (Fig. 1A). Pulses were applied to the tissue phantoms at a pulse repetition frequency (PRF) of 1 Hz, allowing sufficient time for residual nuclei to dissipate before the subsequent pulse arrives. This reduces the possibility of residual nuclei from cavitation from a previous pulse altering the probability of cavitation on a subsequent pulse [10,29]. As described in the previous section, optical imaging monitored cavitation from each pulse. The number of pulses with detected cavitation events out of the total pulses determined the cavitation probability, p_{cav}, for each pressure level.

The cavitation threshold for each experimental case was determined using the 100 captured images according a previously described method [10,11]. The probability of observing cavitation is approximated by a sigmoid function, given by

$$P(p_-) = \frac{1}{2} + \mathrm{erf}\left(\frac{p_- - p_t}{\sqrt{2\sigma^2}}\right) \quad (1)$$

where erf is the error function, p_t is the negative pressure at which the probability $P_{cav} = 0.5$, and σ is a variable related to the width of the transition between $P_{cav} = 0$ and $P_{cav} = 1$, with $\pm\sigma$ giving the difference in pressure from $P_{cav} = 0.15$ to $P_{cav} = 0.85$ for each case tested [10]). MATLAB curve fitting software was employed to analyze all data sets using these parameters. As calculated by the curve fit for each case, the cavitation threshold, p_t, was defined as the $p-$ corresponding to $P_{cav} = 0.5$.

Bubble Cloud Dimensions

The optical imaging system and parameters used for threshold analysis captured one image per pulse of clouds generated at $p-$ ranging from 0 to 18 MPa at 1 Hz PRF inside 1% agarose tissue phantoms containing NCCs. Images were captured of 100 pulses applied to a single focal point inside NCC-containing agarose phantoms for the three dual-frequency cases (−100 ns, 0 ns, and +100 ns) driven by all 32 histotripsy elements in a 1:1 pressure ratio, as well as for the component single frequencies of 500 kHz and 3 MHz (16 elements each). Results are reported as the mean ± the standard deviation of a sample size of 100 bubble clouds per pulsing scheme.

Red Blood Cell Ablation

Red blood cell phantoms were used to characterize the tissue ablation for histotripsy bubble clouds generated from NCCs. Ablation can be directly visualized as the embedded RBC layer turns translucent as the cells are lysed by repeated pulsing [9,16,28,30]. Previous studies have also reported lesions formed in RBC phantoms to be similar to those produced in tissue as identified by histology [9,28,30]. The RBC layer centered on the focus and oriented parallel to the direction of sound propagation. The bubble cloud and resulting ablation were recorded by high-speed optical imaging after each pulse (Fig. 1A**).** Two thousand histotripsy pulses were applied to the RBC phantom at a pressure of 12 MPa for both 1 and 100 Hz PRF experiments, and the camera was triggered twice per pulse to capture the cloud formation and resulting lesion. One image was taken very early in the cloud expansion (3 μs after arrival of the peak negative pressure), and a second was taken of the resulting RBC lesion formed after each pulse once all residual bubbles had dissipated from the field.

Imaging of the 1 Hz PRF case was collected using the FLIR camera and high-speed strobe described earlier with a strobe exposure of 3 µs. The 100 Hz PRF experiments were conducted using a Photron high-speed camera (Nova S12 monochrome, Proprietary Design Advanced CMOS, Photron USA, Inc., San Diego, CA, USA) attached to an 85 mm f/2.8 1 × −5 × super-macro lens (Creator, Mitakon Zhongyi, Liaoning Province, CHN), giving a resolution of ∼4 μm per pixel. Subjects were backlit by a continuous LED light source (Multi-LED QT Light, MultiLED G8 controller, 320 W power supply, GS Vitec, Soden-Salmünster, Germany). Three separate ablations were formed for each experimental case. The ablation area after each recorded pulse was measured using MATLAB, as described previously [6,16,28], to create a plot of ablated area versus pulse number. The ablation areas after each pulse were normalized to the mean area of the respective bubble clouds formed in each case to allow for a comparison of each case's relative ablative efficiency [6,15]. By use of this method, a complete ablation would be defined as the total removal of the mean cloud area of RBCs in the region of the bubble cloud, with the number of necessary pulses representing the ablative efficiency [6,15].

Results

Single- and Dual-Frequency NMH: Bubble Cloud Optical Characterization

High-speed optical imaging was used to visualize histotripsy bubble clouds generated at $p-$ranging from 0 to 18 MPa at 1 Hz PRF inside agarose tissue phantoms containing fluid-filled PFH−NCCs for three dual-frequency cases (−100, 0, and +100 ns), as well as for component single frequencies of 500 kHz and 3 MHz (16 elements each) (Fig. 2). For all phantoms, cavitation bubbles were observed only for pressures greater than ∼9 MPa (Fig. 2). Bubble clouds appeared characteristically as well-defined clouds that increased in size and density with increasing $p-$ similar to clouds produced in previous intrinsic threshold histotripsy studies [6,9–11,15,16] (Fig. 2). Peripheral bubbles started to be observed in regions near but slightly outside of the primary bubble cloud for dual-frequency cases once the applied pressure reached a level approximately twice the NMH cavitation threshold or higher (Fig. 2). In contrast, single-frequency cases retained their characteristic shape at these higher pressures, with two regions of observable bubble density forming with increasing pressure, consisting of a very dense core to the bubble cloud surrounded by a less dense ring of bubbles on the periphery of the cloud. The bubble clouds produced for the three dual-frequency cases appeared to be of similar size to the single-frequency clouds observed at 3 MHz for pressures up to ∼12 MPa. At higher pressures beyond this point, the dual-frequency clouds no longer exhibited the same ellipsoidal dimensions and covered a larger region compared with the 3 MHz cases, although they remained significantly smaller than the 500 kHz bubble clouds (Fig. 2). At these higher pressures, the regions containing cavitation produced by the dual-frequency pulses still matched the region of the focus above the NMH cavitation threshold, with the unique bubble cloud shapes determined by the focal profile of the dual-frequency pulses. The early arrival of the 3 MHz pulse (−100 ns) begins to result in a denser, more concise cloud at higher pressures followed by centered (0 ns) and then late (+100 ns) pulse arrivals, where in these latter two cases increasing areas of peripheral cavitation can be observed toward the front of the cloud.

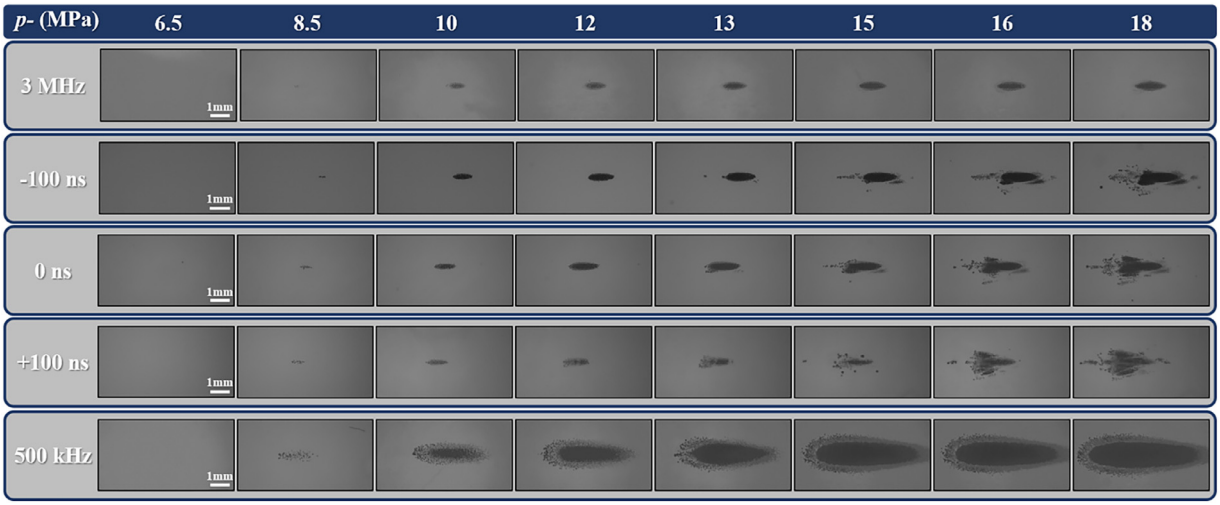

Figure 2. Single- and dual-frequency bubble cloud images. Optical images captured of cavitation bubble clouds generated inside 1% agarose phantoms using the FLIR camera and high-speed strobe from the first histotripsy pulse by 3 MHz single-frequency, three cases of dual-frequency (−100 ns, 0 ns, and +100 ns 3 MHz arrival times) and 500 kHz single frequency shown at the same actual scale. Ultrasound propagation left to right.

Single- and Dual-Frequency NMH: Cavitation Threshold Comparison

The histotripsy cavitation threshold was measured for all 3 MHz arrival times and both single-frequency cases. Figure 3 illustrates the cavitation probability as a function of $p-$ for the three dual-frequency pulsing cases and the two 16-element single frequencies. The measured cavitation threshold for the three dual-frequency (DF) pulsing schemes was $p-_{-100DF}$ = 7.97 MPa, $p-_{0DF}$ = 7.30 MPa, and $p-_{+100DF}$ = 7.74 MPa. Similar cavitation thresholds of $p-_{3\ MHz}$ = 7.22 MPa and $p-_{500\ kHz}$ = 7.47 MPa were observed for the single frequencies. Distinct threshold behaviors with σ_{mean} values <0.4 were observed for all experimental cases, indicating similarities in the NMH threshold behavior between the single-frequency and dual-frequency cases. The overall result indicates a negligible difference in cavitation threshold for different frequencies when using NCCs for NMH.

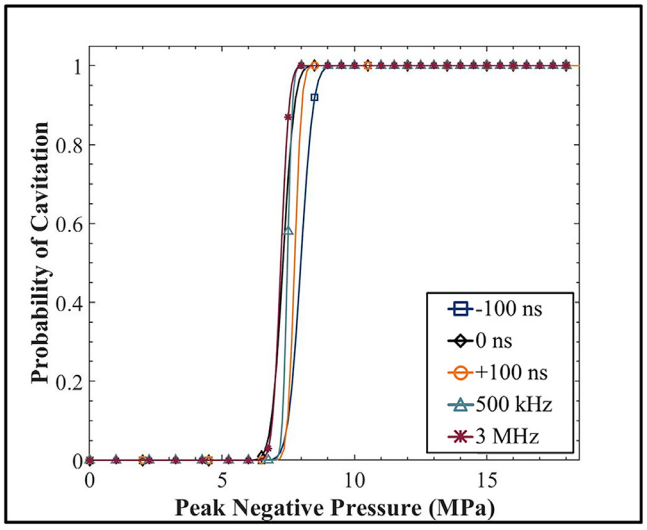

Figure 3. Nanocone cluster (NCC) cavitation threshold curves. Cavitation threshold curves for NCC 1% agarose gels show all dual-frequency conditions exhibit sharp cavitation thresholds. These curves also closely agree with the values for 500 kHz and 3 MHz cavitation thresholds as tested under these conditions.

Single- and Dual-Frequency NMH: Bubble Cloud Dimensions

Bubble cloud dimensions in the axial and elevational directions were measured for all dual-frequency experimental cases and both single frequencies. The bubble cloud area was then calculated using A = (axial diameter/2)(elevational diameter/2)π. The bubble cloud dimensions in the axial and elevational directions and the resulting area (Fig. 4) increased as $p-$ was increased above the respective cavitation thresholds for the pressure range $p-$ = 8.5 MPa to $p-$ = 18.0 MPa. The range of resulting axial and elevation dimensions and the calculated areas are summarized in Table 1. The measured axial (Fig. 4A) and elevational (Fig. 4B) bubble cloud dimensions and calculated areas (Fig. 4C) closely agreed with the 3 MHz cloud size until ~12 MPa of the pressure levels tested. The bubble clouds then began to increase in size, becoming intermediate to the corresponding dimensions for 500 kHz and 3 MHz as $p-$ increased for the tested pressure range. Slight increases in dimensions were observed for the later (+100 ns) arrival of the 3 MHz pulse at pressures greater than ~12 MPa. The results indicated that regardless of arrival time for the 3 MHz pulse for the cases tested, bubble clouds formed using dual-frequency pulsing were closer in dimension to those of the 3 MHz pulse until regions of the 500 kHz beam profile began to surpass the NCC cavitation threshold. Then, the clouds began to become more intermediate in size to the component single frequencies when pulsed at similar $p-$. It should be noted that at pressures greater than 15 MPa, the clouds generated by dual-frequency pulses no longer maintain an elliptical shape so the calculated area (Fig. 4C) may be less accurate at these pressures for the −100, 0, and +100 ns cases. However, the reported maximum axial and elevational measurements are still accurate at these elevated pressures (Fig. 4A,B). Overall, these results indicated the dominant effect of the higher frequency on cloud size until the $p-$ of the individual component frequencies also surpassed the cavitation threshold.

Dual-Frequency NMH Ablation in RBC Phantoms

Agarose tissue phantoms embedded with RBC layers were used to compare the histotripsy ablation capacity for bubble clouds generated from NCCs at different 3 MHz pulse arrival times (−100, 0, and +100 ns). Two thousand histotripsy pulses were applied to a single point in the RBC layer at 1 Hz PRF (Fig. 5) or 100 Hz PRF (Fig. 6) at 12 MPa, with cavitation clouds and resulting lesions captured by optical imaging. The ablated area was confined to regions where cavitation was observed, increasing in total area with increasing pulse number. For

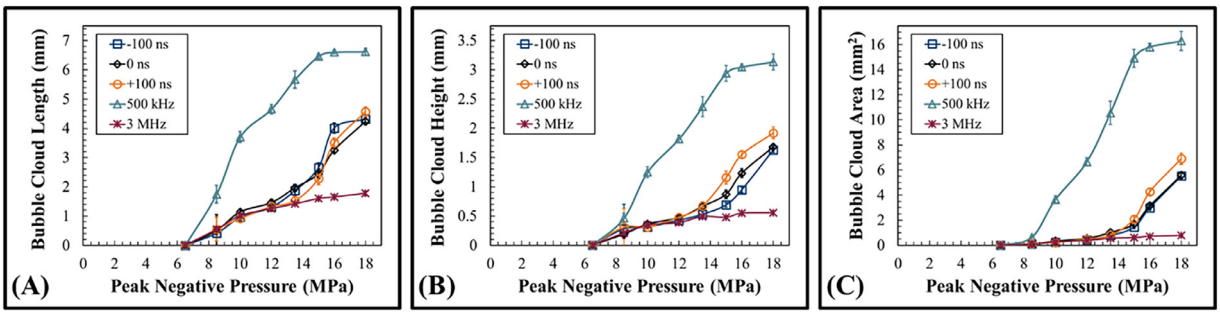

Figure 4. Bubble cloud size comparison. Plots illustrate the measured bubble cloud dimensions in the (A) axial and (B) elevational directions as well as the calculated area (C) using $A = \pi$(axial diameter/2)(elevational diameter/2) between 6.5 and 18 MPa for all dual-frequency cases and for 500 kHz and 3 MHz single frequencies.

Table 1
Range of mean bubble cloud axial and elevational dimensions and calculated cloud area from lowest to highest pressures tested (8.5 and 18 MPa) plus or minus the standard deviation in nanocone clusters containing 1% agarose phantoms.

	Axial (mm)		Elevational (mm)		Area (mm^2)	
	8.5 MPa	18 MPa	8.5 MPa	18 MPa	8.5 MPa	18 MPa
3 MHz	0.54 ± 0.09	1.78 ± 0.07	0.21 ± 0.10	0.55 ± 0.01	0.09 ± 0.05	0.77 ± 0.01
−100 ns	0.42 ± 0.63	4.32 ± 0.14	0.28 ± 0.42	1.63 ± 0.04	0.09 ± 0.2	5.52 ± 0.21
0 ns	0.50 ± 0.12	4.23 ± 0.11	0.19 ± 0.03	1.68 ± 0.04	0.08 ± 0.02	5.58 ± 0.20
+100 ns	0.55 ± 0.41	4.57 ± 0.16	0.31 ± 0.32	1.92 ± 0.11	0.13 ± 0.17	6.90 ± 0.45
500 kHz	1.75 ± 0.3	6.2 ± 0.12	0.46 ± 0.08	3.13 ± 0.14	0.64 ± 0.16	16.29 ± 0.77

1 Hz PRF pulsing, well-defined lesions closely adhering to the size and shape of the bubble cloud confirm results from similar studies using intrinsic nuclei and NCCs [6,15,16,28]. Final lesions were normalized to the mean size of the cloud formed in the RBC phantom to evaluate the rate and efficiency of each 3 MHz arrival time. NMH using NCCs exposed to dual-frequency histotripsy pulsing proved capable of completely ablating the entire focal region <1300 pulses on average for all the tested dual-frequency pulsing parameters, with as few as 350 pulses needed to achieve a complete ablation (Figs. 7 and 8) of the focal area (region containing the bubble cloud following nucleation). This region has previously been reported to closely correlate with the area of the beam profile where the peak negative pressure exceeds the cavitation threshold [6,13,15,29].

Results for 1 Hz PRF experiments inside NCC phantoms revealed clear focal adherence removing areas of RBCs closely matching the size and shape of cloud formed in the phantoms (Fig. 5). Dual-frequency pulsing schemes removed >75% of the focal area in 414.3 ± 217.7, 659.3 ± 350.2, and 623.3 ± 224.2 pulses for −100, 0, and +100 ns 3 MHz pulse arrival times. The lesion size after 2000 pulses had maximum mean areas of 0.49 ± 0.12, 0.62 ± 0.12, and 0.60 ± 0.07 mm^2 for

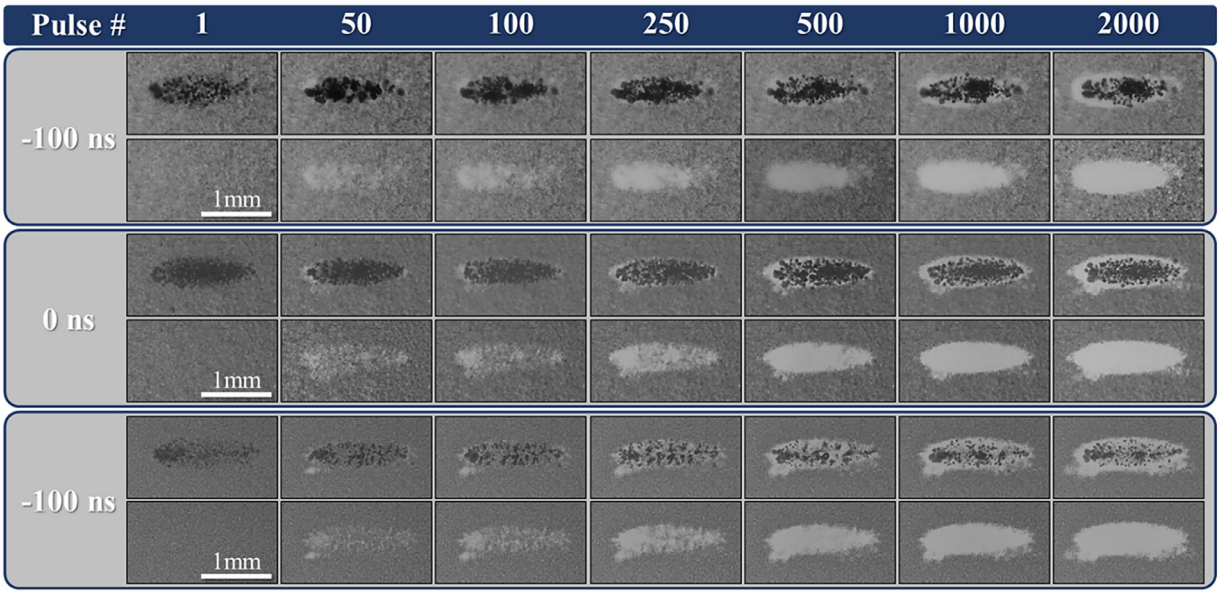

Figure 5. Red blood cell ablation at 1 Hz PRF. Optical imaging using a FLIR camera and high-speed strobe captured images of the cavitation bubble cloud (*dark*) and histotripsy lesions (*white*) generated in red blood cell phantoms (gray) at 1 Hz PRF at 3 MHz arrivals of −100, 0, and +100 ns relative to the arrival of the 500 kHz pulse. Each pair of images comprises the bubble cloud (*top row*) and resulting lesion (*bottom row*) for each designated pulse. Ultrasound propagation left to right. PRF, pulse repetition frequency.

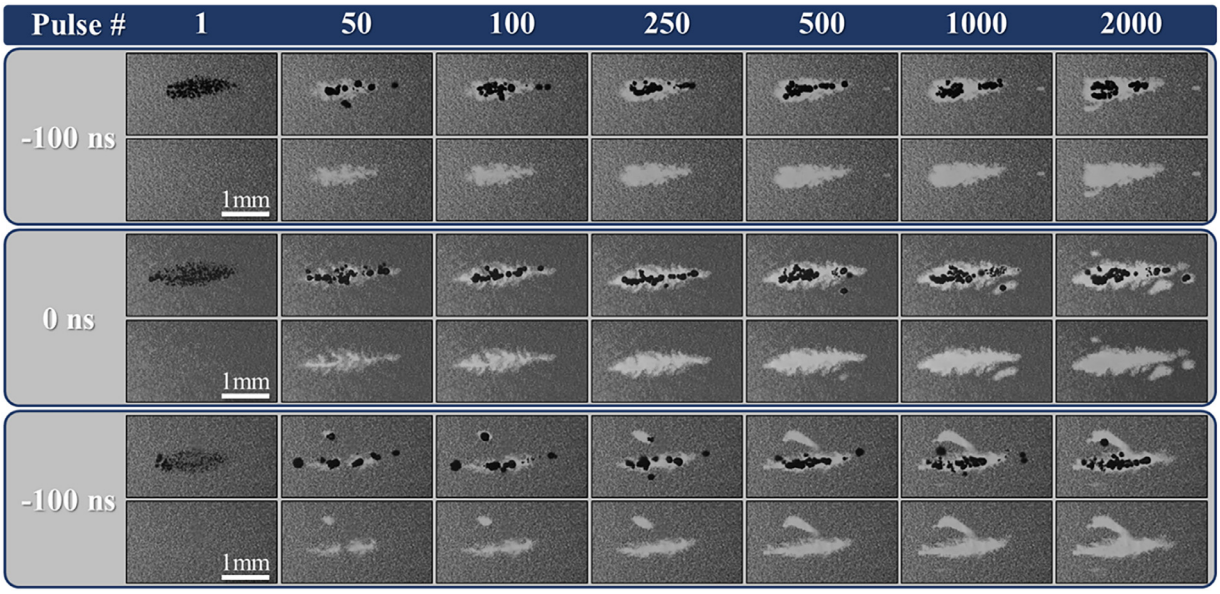

Figure 6. Red blood cell ablation at 100 Hz PRF. High-speed optical imaging using a Photron high-speed camera and continuous LED light source captured images of the cavitation bubble cloud (*dark*) and histotripsy lesions (*white*) generated in RBC phantoms (*gray*) at 100 Hz PRF at 3 MHz arrivals of −100, 0, and +100 ns relative to the arrival of the 500 kHz pulse. Each pair of images comprises the bubble cloud (*top row*) and resulting lesion (*bottom row*) for each designated pulse. Ultrasound propagation left to right.

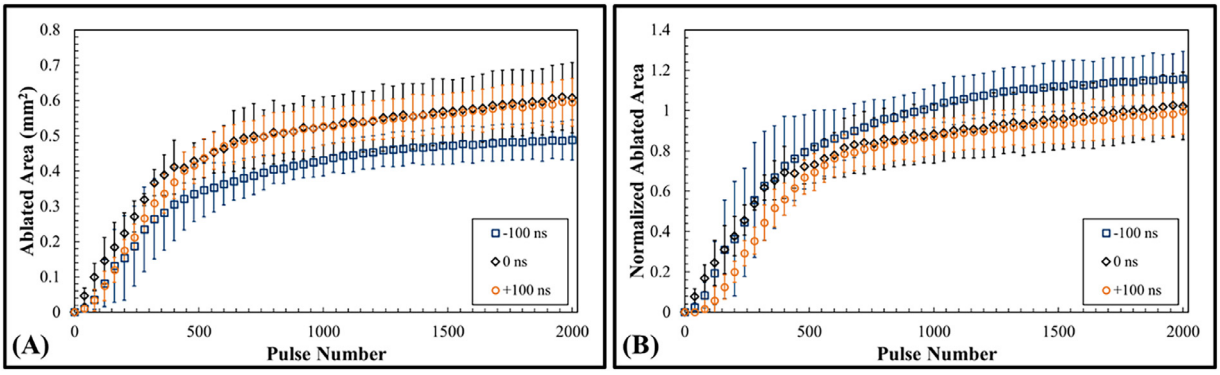

Figure 7. Red blood cell ablation plots: 1 Hz PRF. Mean measured ablation area formed after every 40th pulse (A) and the mean ablation areas normalized to the mean area of the cloud (B) in the red blood cell agarose gel phantoms at 1 Hz PRF histotripsy pulsing. The applied $p-$ was 12 MPa for dual-frequency conditions. PRF, pulse repetition frequency.

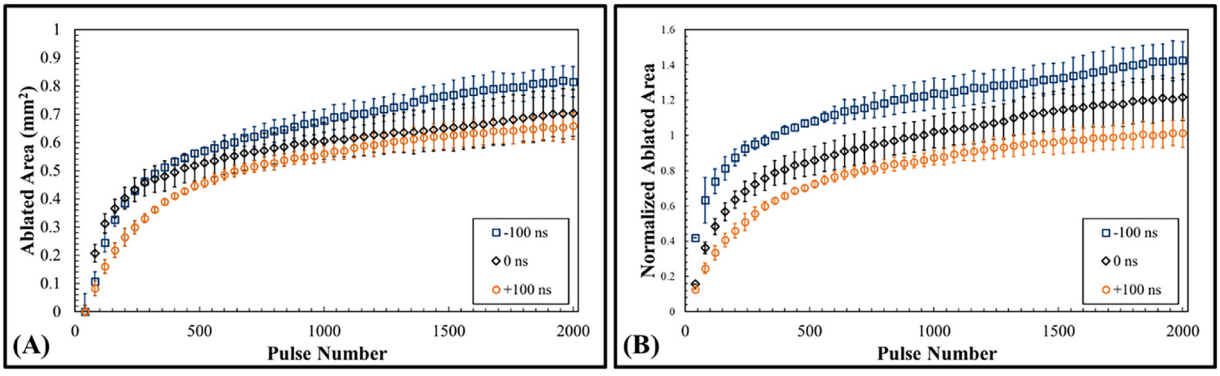

Figure 8. Red blood cell ablation plots: 100 Hz PRF. Mean measured ablation area formed after every 40th pulse (A) and mean ablation areas normalized to the mean area of the cloud (B) in the red blood cell agarose gel phantoms at 100 Hz PRF histotripsy pulsing. The applied $p-$ was 12 MPa for dual-frequency conditions. PRF, pulse repetition frequency.

−100 ns, 0 ns, and +100 ns arrival times, accounting for 116.5 ± 29.3%, 104.6 ± 19.6%, and 100.1 ± 11.8% of the respective mean bubble cloud areas (Fig. 7).

Results for the 100 Hz PRF revealed dual-frequency pulses to be similarly capable of removing an area equivalent to that of the mean bubble cloud area in <2000 pulses, with >75% of the mean cloud area ablated in 128.3 ± 24.0, 333.7 ± 106.3, and 579 ± 60.7 pulses for −100 , 0, and +100 ns, respectively. The resulting maximum mean lesion areas after 2000 pulses were 0.71 ± 0.08, 0.83 ± 0.09, and 0.66 ± 0 .05 mm^2 for −100, 0, and +100 ns, respectively, accounting for 143.7 ± 15.5, 122.6 ± 13.7, and 102.0 ± 8.3% of the mean bubble cloud area (Fig. 8**)**. However, although effective and efficient RBC ablation was achieved, it is important to note that pulsing at 100 Hz PRF (Fig. 6) resulted in less well-defined ablation zones compared with pulsing at 1 Hz PRF. The resulting lesions were larger and more irregular in size and shape, with cavitation damage more evident toward the pre-focal (left) end of the bubble cloud and a greater extent of peripheral damage outside of the main bubble cloud (Fig. 6). These differences in lesion appearance can be attributed to less consistent clouds formations over multiple pulses at the higher pulsing rate (Fig. 6) compared with clouds formed at a 1 Hz PRF (Fig. 5). It is also worth noting that the observed off-target effects were less consistently observed at the 100 Hz PRFs for the −100 ns case, possibly resulting from the more concise, dense clouds observed earlier in the results (Fig. 2).

Discussion

In this study, the bubble cloud behavior and ablative capacity of NMH generated from NCCs exposed to dual-frequency histotripsy was evaluated. NCCs produced stable cavitation capable of creating predictable ablations from histotripsy bubble clouds at a significantly lower *p* −compared with ITH. The repeated cavitation generated from these nuclei over multiple pulses confirms prior studies reporting that these PFH-filled nanoparticles can sustain cavitation to >1000 consecutive pulses. These findings indicate that these nanoparticles can be continually used for the full duration of the applied therapy without needing reperfusion of new particles as would be need for gas-filled cavitation nuclei [6]. Results support our hypothesis that bubble clouds generated from NCCs using dual-frequency histotripsy pulsing produce smaller, more densely populated bubble clouds capable of generating more efficient tissue ablation. The smaller, denser clouds generated by dual-frequency histotripsy in this study overcome the reduction in efficiency for NMH seen in prior studies by forming complete lesions, with the early 3 MHz arrival (−100 ns) cases generating lesions in <500 pulses similar to rates observed for ITH at higher pressures [15]. This increased efficiency can be attributed to the higher bubble cloud density from higher frequency and larger bubble expansion from low frequency seen in the optical imaging above and previously observed in other investigations of dual-frequency histotripsy [22]. The overall findings of this study expand on previous work in developing NMH methods by proposing dual-frequency histotripsy pulsing as method for increasing ablation efficiency dual-frequency pulses at both low and high pulse repetition frequencies.

In the first part of this study, the effects of dual-frequency histotripsy pulsing on the cavitation threshold and bubble cloud characteristics using NCCs for NMH were assessed. The cavitation threshold remained consistent across dual-frequency pulsing regardless of 3 MHz arrival time and closely matched the cavitation thresholds for both 500 kHz and 3 MHz. The consistency of these results suggests that there is minimal to no frequency effect on the NMH cavitation threshold when using NCCs as the nucleating agent. Clouds from all single- and dual-frequency pulsing schemes generated bubble clouds with distinct boundaries that predictably increased in size and number of bubbles consistent with our prior studies on ITH using single- and dual-frequency pulsing [15] as well as our prior work characterizing NMH [5,6]. At pressures directly above the NMH threshold, the size of the dual-frequency clouds closely matched those observed at 3 MHz, suggesting that this “pump-probe” approach [23] can allow for more precise and well-confined NMH ablation. However, at elevated pressures, NMH bubble clouds using dual-frequency pulsing schemes produced areas of varying cloud density, size and shape that repeated pulse to pulse. The irregular shapes and regions of density in the dual-frequency bubble clouds at higher pressures were likely due to partial constructive and destructive inference of the 500 kHz and 3 MHz waveforms in the sound field creating localized regions above the NMH cavitation threshold. For the single-frequency cases, regions of reduced density were observed in a small band surrounding the dense center of the cloud, forming a halo effect. This finding, as well as the unique regions of high and low density in the dual-frequency clouds at the higher pressures, suggests that additional studies are needed to characterize more fully the effects of the focal beam profile on bubble cloud density.

In the final part of this study, we qualitatively evaluated the hypothesis that the NMH ablation efficiency would be improved significantly when exposing NCCs to dual-frequency histotripsy because of the increased cloud density (caused by the higher-frequency component) and enhanced bubble expansion (caused by the lower-frequency component), which was recently established for dual-frequency ITH in a sister study examining these effects for conventional histotripsy using this same experimental setup [22]. Results supported our hypotheses by revealing that all dual-frequency cases significantly exceeded the rate of ablation achieved by single-frequency pulsing in our previous examinations of NMH ablation by generating complete ablations in <1300 pulses compared with the >2000 pulses required in prior studies [1,6]. Unlike our prior investigation of the 500 kHz single-frequency NMH, which found that only ∼70% of the total focal area was removed with 2000 pulses [6], all dual-frequency cases, regardless of pulse arrival time, were capable of ablating areas reflecting the mean area of the cloud for both PRFs tested in this study. At the 1 Hz PRF, dual-frequency pulsing produced well-defined lesions precisely matching the size and location of the cloud, with increasing lesion formation pulse to pulse. Early arrival of the 3 MHz pulse (−100 ns) compared with the 500 kHz pulse produced significantly smaller lesions at significantly faster rates than the centered (0 ns) and late (+100 ns) 3 MHz arrival times, matching a recent study of dual-frequency histotripsy pulsing for ITH [22]. For 100 Hz PRF pulsing, lesions also formed rapidly and achieved complete ablations, with all dual-frequency cases exceeding a total ablated area (>100% of the mean bubble cloud area) within 2000 pulses. These findings are consistent with previous results for NMH using NCCs with single-frequency histotripsy [6] that revealed no overall decrease in ablation efficiency compared with the 1 Hz PRF. However, lesions formed by this higher pulsing rate became more irregular in shape and exhibited a shift toward ablating a larger region at the pre-focal end of the cloud with increased peripheral ablation beyond the focal area [6]. This finding is consistent with other studies of conventional histotripsy that reported higher PRFs result in less precise ablation [30–32].

In addition to decreased lesion precision, these prior studies of higher PRF pulsing in intrinsic threshold histotripsy report a decreased ablation efficiency at higher rates caused by cavitation memory effects [30–32]. This decreased efficiency for higher PRFs was not observed for NMH in this study or prior investigations [6]. We hypothesize that pockets of PFH create an innate “cavitation memory” effect [30,31] that is present for NMH ablation at all PRFs, including very low PRF treatments that would not experience cavitation memory effects from residual gas bubbles. This hypothesis would partially explain the lack of decreased ablation efficiency observed for the higher PRF pulsing in this study. The decreased lesion precision for NMH at higher PRFs can then be accounted for as the PFH aggregations are repeatedly retriggered prefocally and peripherally to the lesion at higher PRFs but are able to localize to the center of the formed lesion at low PRFs. This work presents additional evidence suggesting future work should explore methods for improving NMH and ITH ablation efficiency at higher PRFs while maintaining treatment precision.

Lastly, although the goal of this study was to investigate the effects of dual-frequency pulsing on NMH when using single-cycle pulses, it is worth noting that other studies have been conducted to explore multifrequency pulsing in the context of histotripsy and NMH using longer pulses that rely on mechanisms of action completely different from those proposed here [24,33]. Similarly, there is an extensive body of literature on different types of cavitation agents (microbubbles, nanodroplets, nanocups) being developed for mechanical ablation through focused ultrasound [5,6,24,34]. Although only a single nanoparticle was used in this study, it is likely that the findings of this work will show similar trends when using dual-frequency, single-cycle pulsing with other types of cavitation agents. Future work exploring other multifrequency pulsing methods or other exogenous nucleating agents may enable further optimization of NMH ablation. Both ITH and NMH require further investigation with increasingly refined simulation and quantitative interrogation to fully understand the parameters critical to bubble cloud formation and ablation capabilities. For NMH with NCCs, the current concentration of these particles (10−5 mL PFH/mL water) and efficacy of these techniques have been examined solely *in vitro* [3,6,7]. Future *ex vivo* tissue and *in vivo* investigations using normal NCCs and functionalized NCCs [35] are necessary to establish achievable NCC concentrations, characterize their ablative capabilities in non-agarose media and determine their ability to localize to specific targeted tissue types before their true potential can be determined.

Conclusion

This work investigated the bubble cloud characteristics and ablative capacity of nanoparticle-mediated histotripsy from perfluorohexane-filled nanocone clusters exposed to dual-frequency pulsing using a 500 kHz and 3 MHz dual-frequency transducers. Results revealed that the same distinctive reduction in the histotripsy cavitation threshold was observed for NMH dual-frequency pulsing as was seen in the cavitation threshold for single-frequency pulsing. Results further indicated that NMH from NCCs exposed to dual-frequency pulsing produced more dense bubble clouds capable of precise and complete RBC ablation, with dual-frequency pulsing enabling NMH to ablate the focal area with an efficiency similar to what has previously been reported for conventional histotripsy methods that use higher pressures. Collectively these findings represent a significant advancement for dual-frequency NMH-based therapies that are currently being developed for specific clinical applications requiring localized, targeted therapies.

Conflict of Interest

E.V. and T.L.H. have research and financial relationships with HistoSonics Inc.

Acknowledgments

The research reported in this publication was supported by the National Institute of Biomedical Imaging and Bioengineering of the National Institutes of Health (NIH) under Award No. R21EB027979. The content is solely the responsibility of the authors and does not necessarily represent the official views of the National Institutes of Health. Y.Y.D. was supported by the Scientific & Technological Research Council of Turkey (TUBITAK) for nanocone preparation (Project No. 118Z324).

Data Availability Statement

The raw data supporting the conclusions of this article will be made available by the authors without undue reservation.

References

[1] Vlaisavljevich E, Durmaz YY, Maxwell A, Elsayed M, Xu Z. Nanodroplet-mediated histotripsy for image-guided targeted ultrasound cell ablation. Theranostics 2013;3:851–64.
[2] Yuksel Durmaz Y, Vlaisavljevich E, Xu Z, ElSayed M. Development of nanodroplets for histotripsy-mediated cell ablation. Mol Pharm 2014;11:3684–95.
[3] Khirallah J, Schmieley R, Demirel E, Rehman TU, Howell J, Durmaz YY, et al. Nanoparticle-mediated histotripsy (NMH) using perfluorohexane 'nanocones'. Phys Med Biol 2019;64:125018.
[4] Childers C, Edsall C, Mehochko I, Mustafa W, Durmaz YY, Klibanov AL, et al. Particle-mediated histotripsy for the targeted treatment of intraluminal biofilms in catheter-based medical devices. BME Front 2022;2022:9826279.
[5] Kaymaz Bl, Mustafa W, Hall S, Vlaisavljevich E, Sensoy O, Yuksel Durmaz Y. Experimental and computational investigation of clustering behavior of cyclodextrin−perfluorocarbon inclusion complexes as effective histotripsy agents. Mol Pharm 2022;19:2907–21.
[6] Edsall C, Khan ZM, Mancia L, Hall S, Mustafa W, Johnsen E, et al. Bubble cloud behavior and ablation capacity for histotripsy generated from intrinsic or artificial cavitation nuclei. Ultrasound Med Biol 2021;47:620–39.
[7] Rehman TU, Khirallah J, Demirel E, Howell J, Vlaisavljevich E, Yuksel Durmaz Y. Development of acoustically active nanocones using the host−guest interaction as a new histotripsy agent. ACS Omega 2019;4:4176–84.
[8] Xu Z, Hall TL, Vlaisavljevich E, Lee Jr. FT. Histotripsy: the first noninvasive, non-ionizing, non-thermal ablation technique based on ultrasound. Int J Hyperthermi 2021;38:561–75.
[9] Lin KW, Kim Y, Maxwell AD, Wang TY, Hall TL, Xu Z, et al. Histotripsy beyond the intrinsic cavitation threshold using very short ultrasound pulses: microtripsy. IEEE Trans Ultrason Ferroelectr Freq Control 2014;61:251–65.
[10] Maxwell AD, Cain CA, Hall TL, Fowlkes JB, Xu Z. Probability of cavitation for single ultrasound pulses applied to tissues and tissue-mimicking materials. Ultrasound Med Biol 2013;39:449–65.
[11] Vlaisavljevich E, Lin KW, Maxwell A, Warnez MT, Mancia L, Singh R, et al. Effects of ultrasound frequency and tissue stiffness on the histotripsy intrinsic threshold for cavitation. Ultrasound Med Biol 2015;41:1651–67.
[12] Arvengas A, Herbert E, Cersoy S, Davitt K, Caupin F. Cavitation in heavy water and other liquids. J Phys Chem B 2011;115:14240–5.
[13] Vlaisavljevich E, Aydin O, Lin KW, Durmaz YY, Fowlkes B, El Sayed M, et al. The role of positive and negative pressure on cavitation nucleation in nanodroplet-mediated histotripsy. Phys Med Biol 2016;61:663–82.
[14] Miles C, Doering C, Kripfgans OD. Nucleation pressure threshold in acoustic droplet vaporization. J Acoust Soc Am 2018;143:1835.
[15] Edsall C, Ham E, Holmes H, Hall TL, Vlaisavljevich E. Effects of frequency on bubble-cloud behavior and ablation efficiency in intrinsic threshold histotripsy. Phys Med Biol 2021;66(22).
[16] Vlaisavljevich E, Gerhardson T, Hall T, Xu Z. Effects of f-number on the histotripsy intrinsic threshold and cavitation bubble cloud behavior. Phys Med Biol 2017;62:1269–90.
[17] Mancia L, Vlaisavljevich E, Xu Z, Johnsen E. Predicting tissue susceptibility to mechanical cavitation damage in therapeutic ultrasound. Ultrasound Med Biol 2017;43:1421–40.
[18] Mancia L, Vlaisavljevich E, Yousefi N, Rodriguez M, Ziemlewicz TJ, Lee FT, et al. Modeling tissue-selective cavitation damage. Phys Med Biol 2019;64:225001.
[19] Vlaisavljevich E, Lin KW, Warnez MT, Singh R, Mancia L, Putnam AJ, et al. Effects of tissue stiffness, ultrasound frequency, and pressure on histotripsy-induced cavitation bubble behavior. Phys Med Biol 2015;60:2271–92.
[20] Vlaisavljevich E, Maxwell A, Mancia L, Johnsen E, Cain C, Xu Z. Visualizing the histotripsy process: bubble cloud−cancer cell interactions in a tissue-mimicking environment. Ultrasound Med Biol 2016;42:2466–77.
[21] Bader KB, Holland CK. Predicting the growth of nanoscale nuclei by histotripsy pulses. Phys Med Biol 2016;61:2947–66.
[22] Edsall C, Huynh L, Hall TL, Vlaisavljevich E. Bubble cloud characteristics and ablation efficiency in dual-frequency intrinsic threshold histotripsy. Phys Med Biol 2023;68:225006.
[23] Lin KW, Duryea AP, Kim Y, Hall TL, Xu Z, Cain CA. Dual-beam histotripsy: a low-frequency pump enabling a high-frequency probe for precise lesion formation. IEEE Trans Ultrason Ferroelectr Freq Control 2014;61:325–40.
[24] Glickstein B, Aronovich R, Feng Y, Ilovitsh T. Development of an ultrasound guided focused ultrasound system for 3D volumetric low energy nanodroplet-mediated histotripsy. Sci Rep 2022;12:20664.
[25] Qi T, Jing Y, Deng J, Chang J, Sun W, Yang R, et al. Boiling histotripsy using dual-frequency protocol on murine breast tumor model and promotes immune activation. IEEE Trans Ultrason Ferroelectr Freq Control 2023;70:1773–85.
[26] Zhang D, Wang X, Lin J, Xiong Y, Lu H, Huang J, Lou X. Multi-frequency therapeutic ultrasound: A review. Ultrason Sonochem 2023;100:106608.
[27] Parsons JE, Cain CA, Fowlkes JB. Cost-effective assembly of a basic fiber-optic hydrophone for measurement of high-amplitude therapeutic ultrasound fields. J Acoust Soc Am 2006;119:1432–40.
[28] Maxwell AD, Wang TY, Yuan L, Duryea AP, Xu Z, Cain CA. A tissue phantom for visualization and measurement of ultrasound-induced cavitation damage. Ultrasound Med Biol 2010;36:2132–43.
[29] Vlaisavljevich E, Aydin O, Durmaz YY, Lin KW, Fowlkes B, El Sayed M, Xu Z. Effects of ultrasound frequency on nanodroplet-mediated histotripsy. Ultrasound Med Biol 2015;41:2135–47.

[30] Wang TY, Xu Z, Hall TL, Fowlkes JB, Cain CA. An efficient treatment strategy for histotripsy by removing cavitation memory. Ultrasound Med Biol 2012;38:753–66.
[31] Duryea AP, Cain CA, Roberts WW, Hall TL. Removal of residual cavitation nuclei to enhance histotripsy fractionation of soft tissue. IEEE Trans Ultrason Ferroelectr Freq Control 2015;62:2068–78.
[32] Duryea AP, Cain CA, Tamaddoni HA, Roberts WW, Hall TL. Removal of residual nuclei following a cavitation event using low-amplitude ultrasound. IEEE Trans Ultrason Ferroelectr Freq Control 2014;61:1619–26.
[33] Bismuth M, Katz S, Rosenblatt H, Twito M, Aronovich R, Ilovitsh T. Acoustically detonated microbubbles coupled with low frequency insonation: multiparameter evaluation of low energy mechanical ablation. Bioconjug Chem 2022;33:1069–79.
[34] Kwan JJ, Graham S, Myers R, Carlisle R, Stride E, Coussios CC. Ultrasound-induced inertial cavitation from gas-stabilizing nanoparticles. Phys Rev E Stat Nonlin Soft Matter Phys 2015;92:023019.
[35] Toydemir C, Hall S, Demirel E, Elmaci DN, Gol D, Vlaisavljevich E, et al. Bioconjugated beta-cyclodextrin–perfluorohexane nanocone clusters as functional nanoparticles for nanoparticle-mediated histotripsy. Biomacromolecules 2022;23:5297–311.